Overcoming the Blood–Brain Barrier for Delivering Drugs into the Brain by Using Adenosine Receptor Nanoagonist

Xihui Gao,[†] Jun Qian,[†] Shuyan Zheng,[†] Yinzhi Changyi,[†] Jianping Zhang,[§] Shenghong Ju,[‡,*] Jianhua Zhu,[†] and Cong Li[†,*]

[†]Key Laboratory of Smart Drug Delivery, Ministry of Education, School of Pharmacy, Fudan University, 826 Zhangheng Road, Shanghai 201203, China, [‡]Jiangsu Key Laboratory of Molecular and Functional Imaging, Department of Radiology, Zhongda Hospital, Medical School of Southeast University, 87 Dingjiaqiao Rd., Nanjing 210009, China, and [§]Department of Nuclear Medicine, Fudan University Shanghai Cancer Center, 270 Dong'an Road, Shanghai 200032, China

ABSTRACT The extremely low permeability of the blood–brain barrier (BBB) poses the greatest impediment in the treatment of central nervous system (CNS) diseases. Recent work indicated that BBB permeability can be up-regulated by activating A_{2A} adenosine receptor (AR), which temporarily increases intercellular spaces between the brain capillary endothelial cells. However, due to transient circulation lifetime of adenosine-based agonists, their capability to enhance brain delivery of drugs, especially macromolecular drugs, is limited. In this work, a series of nanoagonists (NAs) were developed by labeling different copies of A_{2A} AR activating ligands on dendrimers. *In vitro* transendothelial electrical resistance measurements demonstrated that the NAs increased permeability of the endothelial cell monolayer by compromising the tightness of tight junctions, the key structure that restricts the entry of blood-borne molecules into the brain. *In vivo* imaging studies indicated the remarkably up-regulated brain uptake of a macromolecular model drug (45 kDa) after intravenous injection of NAs. Autoradiographic imaging showed that the BBB opening time-window can be tuned in a range of 0.5–2.0 h by the NAs labeled with different numbers of AR-activating ligands. By choosing a suitable NA, it is possible to maximize brain drug delivery and minimize the uncontrollable BBB leakage by matching the BBB opening time-window with the pharmacokinetics of a therapeutic agent. The NA-mediated brain drug delivery strategy holds promise for the treatment of CNS diseases with improved therapeutic efficiency and reduced side-effects.

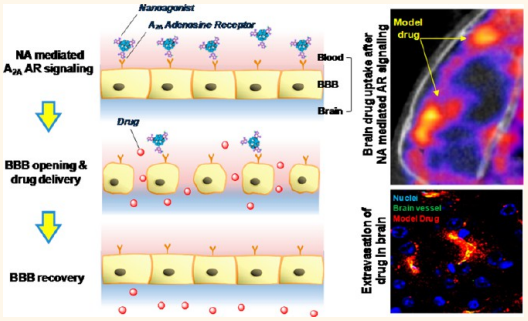

KEYWORDS: nanoagonist · blood–brain barrier · adenosine receptor · brain drug delivery · multimodal imaging

Treatments for central nervous system (CNS) diseases are limited by the inadequacy in delivering therapeutic agents to the desired locations. The extremely low permeability of the blood–brain barrier (BBB) is a main reason leading to compromised brain drug delivery and therapeutic efficiency.[1] For example, of the more than 7000 drugs analyzed in the Comprehensive Medicinal Chemistry (CMC) database, only 1% of them showed BBB permeability and activity in the CNS.[2] As a unique physiological structure of the blood vessels in the brain, the BBB precisely regulates the movement of molecules, ions, and cells between the blood and brain tissue[3] and plays an important role in maintaining a precisely controlled microenvironment for proper functionalities including neuronal circuits, synaptic transmission, synaptic remodeling, angiogenesis, and neurogenesis.[4] The BBB restricts the entry of molecules into the brain through two main strategies. First, tight junctions (TJs) seal the endothelial cells and induce a high intercellular electrical resistance (1000–2000 Ω cm^2), which leads to an extremely low permeability to blood-borne molecules.[5] Second, compared to endothelial cells in peripheral vasculatures, there are few transcellular transport pathways but high expression levels of active efflux transport proteins such as P-glycoprotein (P-gp) on brain capillary endothelial cells (BCECs).[3] As a result, the overwhelming majority of small molecules and almost all macromolecules do not cross the BBB.[6,7] Therefore, there is great need for a safe and effective method to facilitate

* Address correspondence to congli@fudan.edu.cn; jsh0836@hotmail.com.

Received for review January 18, 2014 and accepted March 27, 2014.

Published online March 27, 2014
10.1021/nn5003375

brain delivery of drugs for the treatment of CNS disorders.

Even though local BBB disruption is observed in CNS diseases such as brain tumor,[8,9] ischemia stroke,[10,11] Alzheimer's disease,[12] and Parkinson's disease,[13] this does not necessarily imply efficient intracerebral drug delivery. The presence of multiple drug-resistance mechanisms,[14] high intracranial pressure, and heterogeneous perfusion rate lead to the drug concentration in lesions far less than the threshold for therapy.[15] Current strategies for brain drug delivery include intracranial injection, disrupting the BBB *via* chemical or physical approaches, and traversing the BBB *via* biological strategies. Intracranial injections such as convection-enhanced delivery (CED)[16,17] deliver the drug directly into the lesions. However, the prerequisite to precisely locate the focus, low drug diffusion rates in brain parenchyma, and potential physical injury limit their applications in the clinic. Hypertonic chemicals such as mannitol induce osmotic pressure between the vascular wall, break the TJs, and increase BBB permeability.[18] Nevertheless, the chemical strategy carries the risks of neurotoxicity[19] and epileptic seizures[20] due to TJ leakage. Focused ultrasound (FUS) locally disrupts the BBB[21] *via* a thermal coagulative effect or microbubble oscillation.[22] Even FUS was reported to increase therapeutic efficacy of gliomas,[15,22] the limited focal depth (<3 cm), the requirement for image-guidance, and the thermally induced irreversible BBB recovery need to be overcome. Transcytosis is a biological pathway by which endogenous macromolecules traverse endothelial cells within endocytic vesicles from the luminal side to the abluminal side where exocytosis occurs.[23] However, the transcytosis approach suffers from low receptor expression level, limited endocytic events, and the prerequisite for labeling cationic groups[24] or receptor targeting ligands[25,26] on the drug or drug delivery vectors. Therefore, it is necessary to develop a new brain drug delivery strategy with high efficacy, minimized neurological injury, and tolerance to molecular weights and pharmacokinetics of drugs.

Considering the key role of TJs played in restricting the entry of molecules into the brain, reversibly changing TJs' tightness may be a feasible way to adjust BBB permeability. Adenosine receptors (ARs) are a class of G protein-coupled receptors (GPCRs) and have four subtypes, A_1, A_{2A}, A_{2B}, and A_3, which are actively involved in diseases such as inflammation, cancer, cardiovascular damage, and nervous system disorders[27] Bynoe *et al.* recently demonstrated that the specific activation of A_{2A} AR on mouse BCECs could facilitate brain drug uptake.[28] Even the downstream players of the agonist-modulated A_{2A} AR signaling have not been clearly elucidated. The AR signaling changes cytoskeletal elements by regulating intracellular actin dynamics,[29] which leads to contractions in cell morphology, loss of TJ integrity, and increase of the barrier permeability. Although numerous adenosine-based agonists with high binding affinity and specificity to A_{2A} AR were developed,[30] their capability for facilitating brain drug delivery is hindered by their transient circulation lifetime (5 s to 5 min), which results in the compromised CNS uptake of drugs, especially for macromolecular therapeutics such as antibodies and nanosized drug delivery systems.

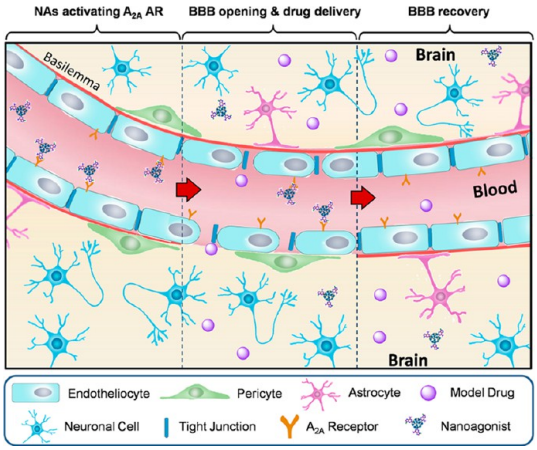

Figure 1. Overview of brain drug delivery by up-regulating BBB permeability *via* NA-mediated A_{2A} AR signaling. The NA specifically activates the A_{2A} AR on BCECs. The intracellular signal transduction leads to cytoskeleton modulation, cell shape contraction, and intercellular space enhancement. Drug is given when the BBB permeability is imaged to reach its maximum. The recovery of BBB tightness after receptor signaling minimized side-effects.

Compared to small molecules, nanoparticles demonstrate advantages in pharmaceutical applications including their tunable circulation lifetimes and adjustable receptor binding affinities.[31] In this work, we developed a series of nanoagonists (NAs) that were defined as nanoparticles functionalized with GPCR-activating ligands. The strategy of brain drug delivery *via* the NA-mediated A_{2A} AR signaling is achieved with three steps (Figure 1). First, the NAs specifically activate the A_{2A} AR on BCECs, which initiates intracellular signal transduction and leads to TJ opening. Second, drug is given when the BBB permeability is noninvasively imaged to reach its maximum. Third, the timely recovery of TJ integrity minimizes the side-effects induced by uncontrollable BBB leakage. This strategy holds potential to up-regulate brain drug delivery by enhancing the AR-mediated signal transduction efficacy due to the prolonged circulation lifetime and multivalent effect of NAs.

The rapid development of molecular imaging provides an unprecedented opportunity to noninvasively assess the biological and pathological processes in living subjects at the molecular or cellular level.[32] In this work, the labeling of imaging reporters on both NA and model drug makes it possible to monitor the NA-mediated TJ opening and cerebral delivery of the

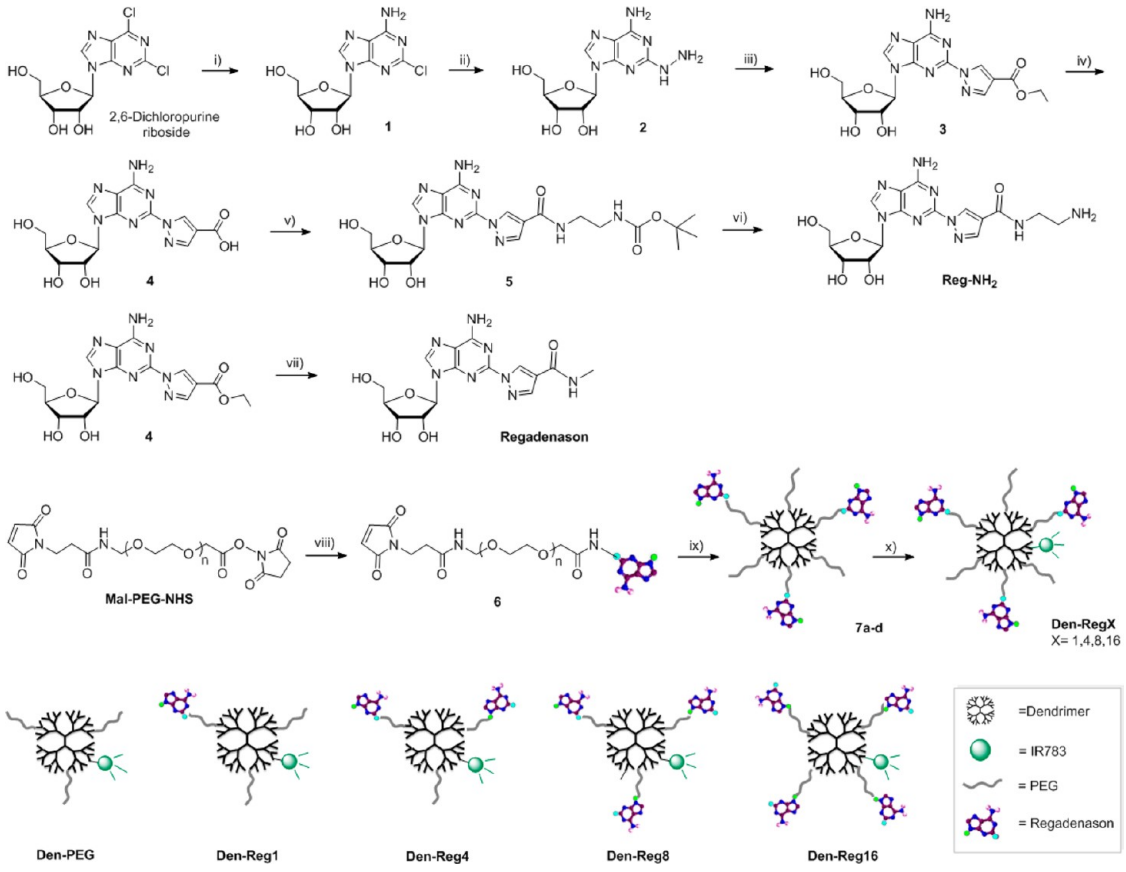

Scheme 1. Synthesis of the NAs: (i) NH_3/MeOH/CH_2Cl_2; (ii) hydrazine hydrate; (iii) ethyl 2,2-diformylacetate/ethanol; (iv) KOH/MeOH; (v) *N*-Boc-ethylenediamine, HBTU/HOBT/DMAP/DMF; (vi) TFA/CH_2Cl_2; (vii) methylamine; (viii) Reg-NH_2/DMF; (ix) G5 dendrimer/PEG-NHS/PBS (pH 7.4); (x) IR783-NHS/HEPES (0.1 M, pH 8.3).

model drug simultaneously by optical imaging and single-photon emission computed tomography/computed tomography (SPECT/CT) imaging. Considering the high sensitivity of optical imaging and the capability of SPECT/CT to offer both anatomical and molecular information, the combination of the above imaging modalities benefits the timed drug delivery when the BBB permeability was imaged to reach its maximum after the NA-mediated AR signaling.

RESULTS

Design, Synthesis, and Characterization of Nanoagonists and Model Drug. The fifth generation (G5) poly(amidoamine) (PAMAM) dendrimer was chosen as a scaffold of the NAs due to its globular architecture, optimized particle size, and well-defined reactive groups on the particle surface.[33] Regadenoson (Lexiscan) is an A_{2A} AR-specific agonist that was approved by the FDA as a coronary vasodilator for radionuclide myocardial perfusion imaging. Even though regadenoson (Reg) has a moderate binding affinity (K_i = 290 nM) to human A_{2A} AR,[27] it produces an equivalent response but a more rapid action termination than high-affinity agonists.[30] In this work, the reactive derivative of Reg were modified on NAs through extended poly(ethylene glycol) (PEG) linkers, which not only significantly improve the biocompatibility of the NAs but also minimize the steric hindrance of the bulky nanoscaffold to the agonist-initiated signal transduction (Scheme 1). Furthermore, near-infrared (NIR) fluorophore IR783 was labeled on NAs to track their distribution *in vivo* because tissue absorption and autofluorescence in the NIR wavelength region (650−900 nm) are low, which allows the NIR light to penetrate into deep tissues. Meanwhile, due to its excellent biocompatibility, nonimmunogenicity, and long circulation lifetime, PEGylated dextran labeled with radioactive ^{99m}Tc-DTPA chelator and rhodamine fluorophore (Figure S1) was used as a model drug[28,34,35] to evaluate brain delivery of macromolecular drugs by SPECT/CT and optical imaging. The molecular weight, hydrodynamic diameter, and surface charge of the model drug were determined as 45 kDa, 7.4 nm, and +8.4 mV, respectively (Figure S2).

The synthesis of NAs Den-RegX (X = 1, 4, 8, 16) and control nanoparticle Den-PEG is outlined in Scheme 1. Briefly, treatment of 2,6-dichloropurine riboside with NH_3/MeOH in a sealed glass tube gave **1**. Reaction of **1** with hydrazine monohydrate afforded adenosine derivatives **2**. Compound **3** was obtained by condensation of **2** with malonaldehyde. Hydrolysis of **3** obtained **4**, which was coupled with *N*-Boc-ethylenediamine in the presence of HBTU/HOAT to give **5**. Deprotection of **5** in

TABLE 1. Physical Parameters of the NAs

nanoagonist	*d* (nm)[a]	PDI[a]	ζ (mV)[a]	Den/PEG/Ago[b]	IC_{50}
Reg	n.d.[d]	n.d.[d]	n.d.[d]	n.d.[d]	4.27 μM
Den-PEG	6.713	0.133	11.6	1/10/0	n.d.[d]
Den-Reg1	7.077	0.284	8.39	1/13/1.6	5.79 μM
Den-Reg4	7.548	0.177	7.24	1/12/4.4	3.75 μM
Den-Reg8	7.692	0.223	6.79	1/12/8.3	1.57 μM
Den-Reg16	7.967	0.271	6.04	1/16/16.7	551 nM

[a] Diameters (*d*), polydispersity index (PDI), and zeta potentials (ζ) were measured by dynamic light scattering (DLS). [b] The molar ratios of dendrimer/PEG/agonist of the NAs were determined by ^{1}H NMR. [c] IC_{50} of the NAs to A_{2A} AR were measured by receptor competitive binding studies on bEnd.3 cells. [d] n.d. means not detected.

trifluoroacetic acid gave the reactive A_{2A} AR ligand Reg-NH_2. Meanwhile, regadenason as a positive control was prepared by reaction of **4** with methylamine. Mal-PEG-NHS (2 kDa) reacted with Reg-NH_2 to give **6**. The treatment of G5 dendrimer (29 kDa) with different molar equivalents of **6** gave **7a**−**d**. Finally, reaction of homemade IR783-NHS with **7a**−**d** respectively gave NAs Den-RegX (X = 1, 4, 8, 16).

The physical parameters of the NAs are listed in Table 1. The hydrodynamic diameters of the NAs were determined to be in the range 7.0−8.0 nm, and their surface charges were measured between +6.0 and +8.4 mV. The polydispersity indexes (PDIs) of all NAs were less than 0.3, and all NAs migrated as a single band in the fluorescence images of the resolved sodium dodecyl sulfate-polyacrylamide gel electrophoresis (SDS-PAGE), which verifies their narrow size distribution (Figure S3). Notably, while the average molar ratios of ligand/dendrimer were measured as 1.6, 4.4, 8.3, and 16.7 for Den-Reg1, Den-Reg4, Den-Reg8, and Den-Reg16, respectively, their PEG/dendrimer ratios stayed around 12−16, which benefits maintaining similar particle size and zeta potential of the NAs.

Nanoagonist Compromise of TJ Tightness of the Cell Monolayer *in Vitro*. The expression of A_{2A} AR in BCECs is a prerequisite for modulating BBB permeability *via* agonist-mediated signaling. A_{2A} AR in mouse brain endothelial bEnd.3 cells was obvious with evidence of an immunoreactive band at 45 kDa, the anticipated molecular weight of A_{2A} AR (Figure 2A). The IC_{50} (50% inhibitory concentration) values of the NAs to A_{2A} AR were measured *via* receptor competitive binding assay, in which NAs bind to A_{2A} AR competitively with the antagonist ^{125}I-ZM241385 (K_i = 0.8 nM)[36] in a concentration-dependent manner (Figure 2B). The receptor binding affinities of NAs increased with their ligand density, and Den-Reg16 was 7.7-fold more potent (IC_{50} = 551 nM) than the monomeric Reg. Treatment of Den-Reg16 led to the formation of actinomyosin stress fiber (ASF) in bEnd.3 cells (Figure 2C). A similar phenomenon was also observed in the cells treated with Reg but not Den-PEG or phosphate-buffered saline (PBS). Considering that ASF is the major mediator of cell motility and contraction,[37] the above results suggest the activation of A_{2A} AR by NAs, leading to cytoskeleton reorganization in BCECs. To investigate TJ integrity after NA-induced cytoskeleton modulation, TJ-associated protein ZO-1, which links cell adhesion molecules to the actin cytoskeleton[38] for maintaining morphology of endothelial cells, was immunostained. While ZO-1 protein was expressed as a continuous alignment on the cell−cell interface, the discontinued intervals and even the full absence of this protein were demonstrated after treatment of Reg or Den-Reg16 (Figure 2D). The above data indicated the compromised TJ tightness after the NA-mediated AR signaling.

Nanoagonist Up-regulation of Cell Monolayer Permeability *in Vitro*. The capability of NAs to modulate BBB permeability was first studied by measuring the transendothelial cell electrical resistance (TEER) values of the mouse brain capillary endothelial bEnd.3 cell monolayer by *in vitro* Transwell assays (Figure 3A). The decreased TEER values had been associated with increased intercellular space and barrier permeability of the cell monolayer.[27] All the NAs led to remarkable TEER value reductions, and the minimal values were observed at 45 min post-treatment (Figure 3B). Notably, while the maximal TEER reduction of Reg was determined as 30% and was independent of its concentration (1−500 μM, Figure S4), the values of NAs increased proportionally to their ligand density, and Den-Reg16 offered the maximal reduction of 68%. Importantly, the time-window of TEER reduction also correlated with the ligand density on the NAs. While less than a 20 min period (>30% TEER reduction) was monitored after Reg treatment, the time-windows induced by NAs increased from 30 min of Den-Reg1 to 2.8 h of Den-Reg16 (Figure 3C). Additionally, the monolayer-traversing efficiency of the macromolecular model drug (45 kDa) increased substantially after pretreatment of the NAs. Den-Reg16 offered the highest model drug crossing efficiency, which was 17.6 and 4.6 times higher than that of saline or Reg (Figure 3D).

Nanoagonist Up-regulation of Model Drug Brain Uptake *in Vivo*. Figure 4A demonstrated *in vivo* near-infrared and rhodamine fluorescence images of nude mice with intact BBB at 2 and 24 h after intravenous (iv) administration of the model drug that was injected at 30 min postinjection (PI) of Den-Reg16 or Den-PEG. Den-Reg16 showed not only much higher cerebral delivery than Den-PEG but also significantly up-regulated model drug uptake in the brain. The above result was verified by the fluorescence images of excised whole brain at 2 and 24 h PI of the model drug (Figure 4B). Additionally, good co-localization between the fluorescence of NA and model drug was observed, which implies the predominant entry of the model drug in the area where the BBB is compromised by NA. In contrast, the brain uptakes of both Den-PEG and its associated model drug remained low in the whole imaging procedure, which

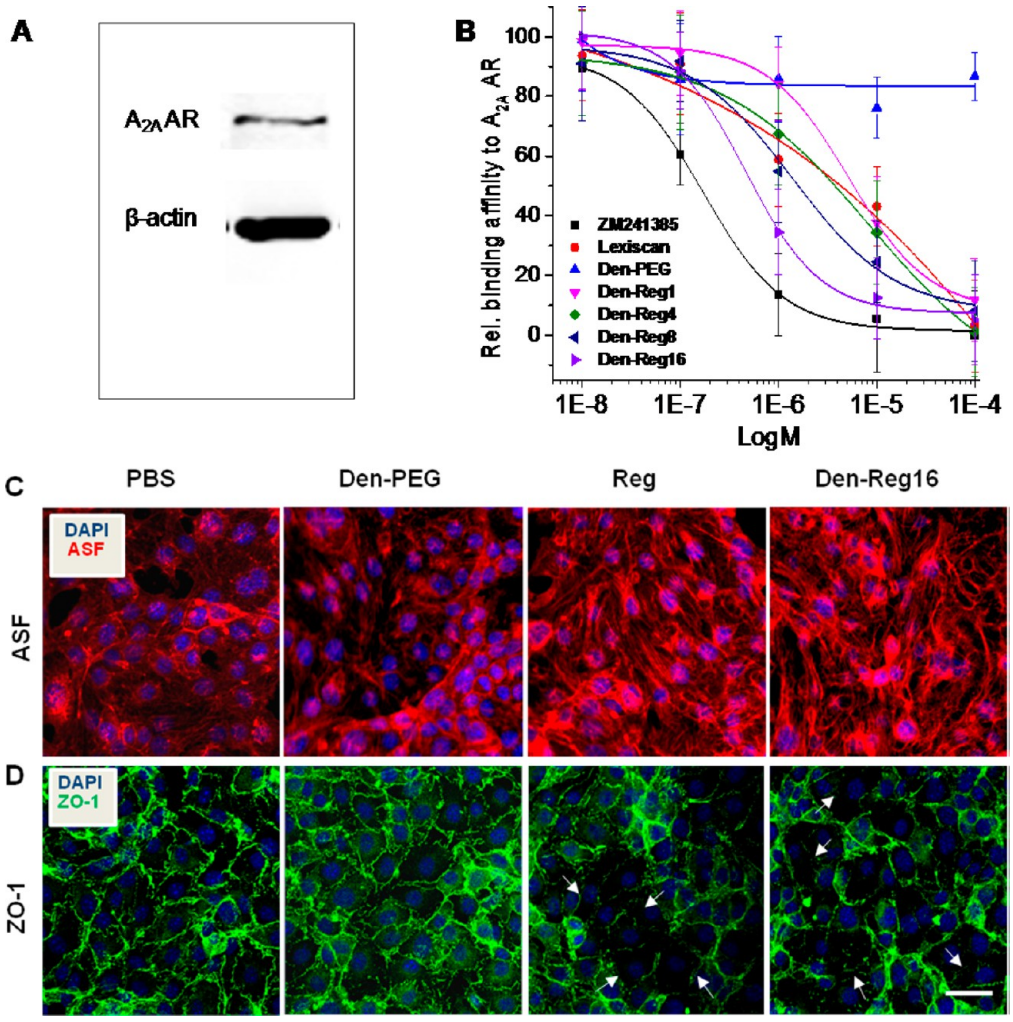

Figure 2. NAs compromising TJ tightness *via* A_{2A} AR-mediated signal transduction. (A) Western blot demonstrates A_{2A} AR expression on bEnd.3 cells. (B) Competitive binding with A_{2A} AR in bEnd.3 cells between ^{125}I-ZM241385 (antagonist) and NAs with different concentrations (n = 4, mean ± SD). (C) Confocal fluorescence microscopic images of bEnd.3 cells stained by phalloidin after treatment with PBS, Reg, or NA (10 μM) for 45 min. Actinomyosin stress fiber (ASF) is displayed in red, and DAPI-stained nuclei are displayed in blue. (D) Immunofluorescence microscopic images of TJ-associated protein ZO-1 after 45 min treatment with PBS, Reg, or NA (10 μM). ZO-1 is displayed in green and nuclei are blue. Arrows indicate disrupted ZO-1 expression on cell interfaces. Scale bar, 50 μm.

confirms the increased BBB permeability after NA-mediated AR signaling. Strong fluorescence of both Den-PEG and Den-Reg16 was observed in the kidney at 2 h PI, which implies their excretion through renal filtration (Figure 4A). At 24 h PI, Den-Reg16 demonstrated a wider distribution area than Den-PEG. This phenomenon can be explained by the nonspecific A_{2A} adenosine receptor signaling following extravasation of Den-Reg16 because of the expression of A_{2A} AR in peripheral tissues/organs.[39] Figure 4C demonstrates time-dependent brain uptake of NA and model drug, respectively, by measuring their fluorescence intensities on mouse brain areas. Much higher uptakes of Den-Reg16 and its associated model drug than those of Den-PEG were observed, which verifies the NA-mediated BBB permeability enhancement.

Brain Drug Delivery *via* NA-Mediated TJ Compromising. Figure 5A demonstrated *in vivo* SPECT/CT images of mouse brains with intact BBB at the sagittal, transversal, and coronal planes when ^{99m}Tc-DTPA-labeled model drug was injected at 30 min PI of saline, Reg, Den-PEG, or Den-Reg16. Intensive radioactivity of the model drug was indicated inside the mouse skull defined by the CT after pretreatment with Den-Reg16, which was quantified as 6.8 and 3.2 times higher than the brains pretreated with saline or Reg. Model drug predominately distributed along the main intracranial vasculatures including the transverse sinus, superior sagittal sinus, and inferior cerebral vein, which implies its extravasation after the NA treatment (Figures 5A and S5). Notably, a trace amount of radioactivity was also observed in the brain treated with saline. This could be explained by the compromised BBB after the inhalation of anesthetics such as isoflurane.[40] Biodistribution studies demonstrated that Den-Reg16 offered the highest macromolecular model drug uptake in whole brain

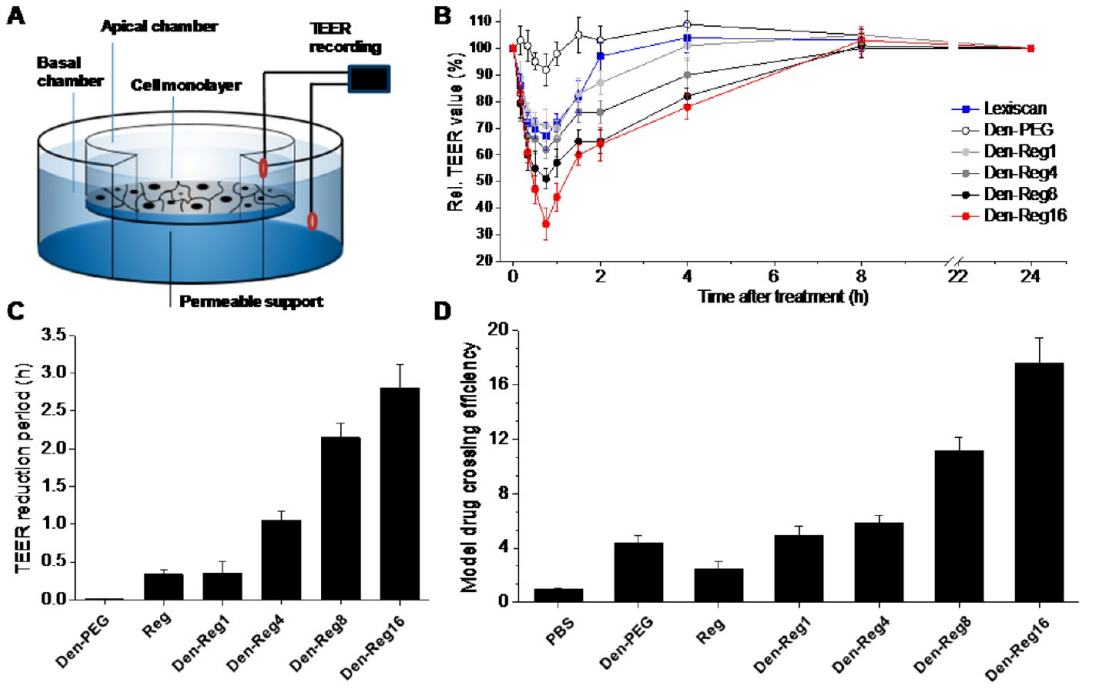

Figure 3. NAs up-regulation of permeability and drug traversing efficiency of the bEnd.3 cell monolayer. (A) Schematic of the Transwell assay to evaluate cell monolayer permeability by measuring the electrical resistance between the electrodes in apical and basal chambers. (B) Time-dependent TEER values measured immediately after addition of 10 μM NA, which was removed 45 min after treatment (n = 8, mean $\pm$ SD). 10 μM Den-PEG and Reg were used as negative and positive controls, respectively. (C) Time-windows of TEER value reduction after NA treatment (>30% reduction). (D) Normalized monolayer traversing efficiency of the model drug. The monolayer was treated with 10 μM NA for 45 min. After removing the NA, the model drug was added and incubated for 8 h. The monolayer crossing efficiencies were determined by quantifying the model drug fluorescence in the basal chamber (n = 4, mean $\pm$ SD).

with a value of 0.13 $\pm$ 0.015 %ID/g, which was about 8.5 and 3.1 times higher than that treated with saline or Reg (Figure S6). Notably, the highest model drug uptake was found in the lung (34.2 $\pm$ 9.5 %ID/g, Figure S7), which could be explained by the nonspecific attachment of the positively charged model drug (Figure S2A) on pulmonary vasculatures *via* electrostatistic affinity after iv injection. Additionally, avid phagocytosis of macrophages[41] may further accelerate the pulmonary accumulation of the model drug. Immunofluorescence microscopic imaging studies clearly demonstrated the Den-Reg16-mediated brain drug delivery (Figure 5B). The extravasation of the model drug was evident in the cortex, striatum, and cerebellum areas, and the drug distributed as tiny vesicles with a concentration-decreasing gradient from the vasculatures immunostained by CD31 antibody to the extracellular matrix. In contrast, residue model drug was found in the striatum and cerebellum after pretreatment with Den-PEG, but it was exclusively located inside the vessels, which indicates the uncompromised BBB tightness (Figure 5C).

Nanoagonist Tuning of the BBB Opening Time-Window. The BBB opening time-windows were studied by measuring model drug brain uptake when the drug was injected at selected time-points after NA administration. Figure 6A shows the photographic and corresponding radioautographic images of brain sections in which the model drug uptake was evident, with high radioactivity displayed in dark color. While the radioactivity stayed at background level after Den-PEG treatments, the entries of model drug in the brain were obvious upon pretreatment with NAs or Reg. Notably, all NAs led to a faster BBB permeability enhancement compared to Reg. While the intense brain uptake of model drug was observed when it was injected at 10 min PI of NAs, the entry of model drug was not observed until 30 min after Reg injection. NAs also prolonged the BBB opening time-windows, which increased proportionally with their ligand density. Figure 6B shows the time-course of intracerebral drug delivery efficiency after the preinjection of NAs or Reg. For example, obvious model drug uptake was observed when it was injected at 30 min and 1 h but not at 10 min or 2 h PI of Reg, which indicates the BBB opening time-window of Reg is at least 30 min. Similarly, the corresponding time-windows of Den-Reg1, Den-Reg4, Den-Reg8, and Den-Reg16 were determined to be at least 1, 1, 2, and 2 h. Notably, the BBB tightness was recovered after treatment with the NAs, which is important to reduce the potential risk of uncontrollable BBB leakage.

DISCUSSION

The BBB restricts the access of blood-borne molecules into the brain *via* TJs that seal the BCECs with an extremely low permeability as well as a high electrical

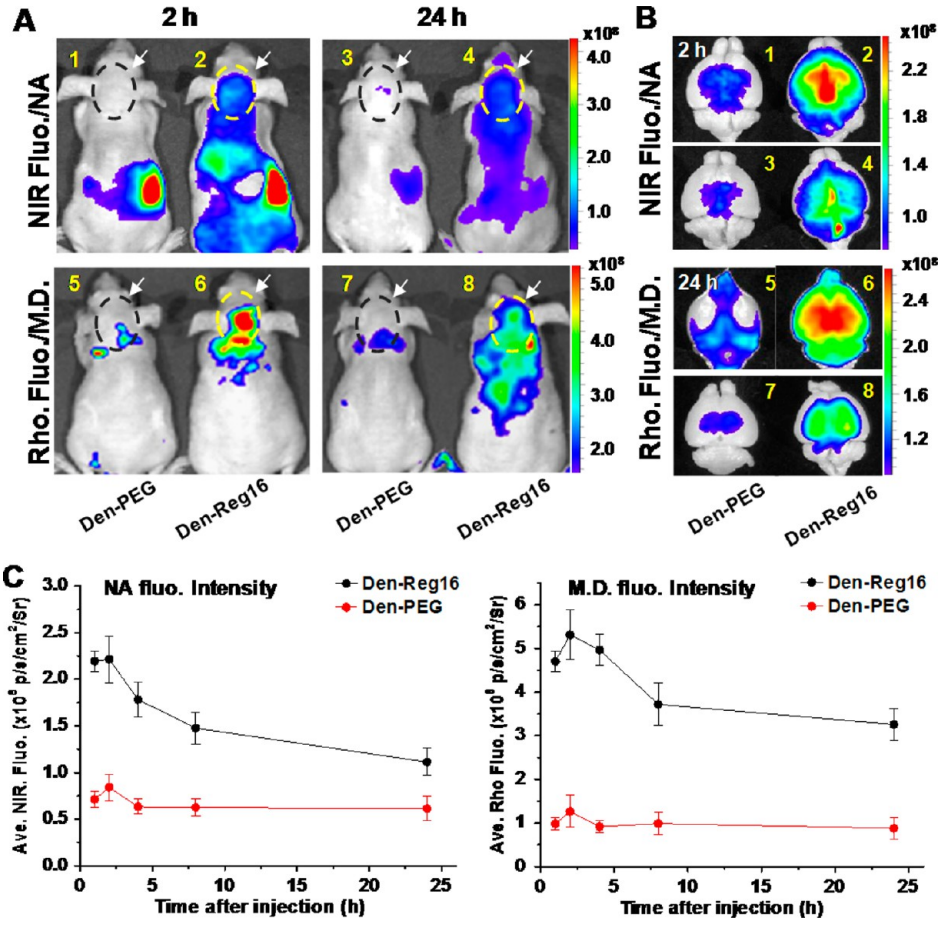

Figure 4. NA up-regulation of model drug brain delivery in mice with intact BBB. (A) *In vivo* optical images of NA (NIR fluo.) and model drug (rhodamine fluo.) at 2 and 24 h PI of Den-Reg16 or Den-PEG (10 nmol/mouse). Mouse brain areas are indicated by arrow-pointed circles. (B) *Ex vivo* optical images of NA and model drug in excised mouse brains at 2 and 24 h PI of NA. (C) Time-dependent fluorescence intensities of NA (left panel) and model drug (right panel) on mouse brain area at 2 and 24 h PI of NA *via* iv (n = 4, mean ± SD). Model drug (1.0 mg/mouse) was always injected at 30 min PI of NA *via* iv.

resistance. Temporarily opening TJs is a feasible way for brain drug delivery because of its high efficiency and tolerance to molecular weights of therapeutics. Even hypertonic agents such as mannitol were reported for the treatment of brain tumors[37] and Alzheimer's disease[42] by breaking TJs *via* osmotic pressure. Their main application in the clinic is to reduce intracranial pressure in emergency circumstances before more definitive treatments are applied. Moreover, the high dosage (1.0−2.0 g/kg), fixed BBB opening time-window (≈30 min),[43] and the potential risk induced by leaky TJs limit its applications. AR agonist mediated TJ opening has attracted attention recently because of its ultrahigh efficiency (0.5−50 μg/kg)[28] and rapid TJ recovery, which attenuates potential side-effects. However, the rapid excretion rate of the agonists leads to a narrow BBB opening time-window and low brain drug delivery efficiency. Therefore, NAs with prolonged circulation lifetime and improved receptor signaling efficacy are the method of choice to address the above challenges.

To label the AR-activating ligands on the nanocarrier, a reactive intermediate, Reg-NH_2, was prepared. It has an identical AR-activating structure to Reg except for the introduction of a primary amine at the terminal of purine C2 substitution for conjugation convenience. A straightforward synthetic strategy (Scheme 1) was developed to prepare Reg-NH_2, which not only avoids the tedious protection and deprotection on the hydroxides in ribose[44] but also offers an overall yield above 20%. Even though maleimide shows much lower reactivity to amines than that to sulfhydryl, we indeed found a very efficient coupling between PAMAM dendrimer and the maleimide derivative under pH 7.4−8.3. This phenomenon could be explained by (1) the decreased pK_a values of the amidoamines (7.7−9.5) on the dendrimer periphery compared to that of aliphatic primary amines (9.9−11.1)[45] and (2) the high local concentration of terminal amidoamines on the dendrimer surface (128 amidoamines per G5 dendrimer). Due to the high coupling efficiency, the number of AR-activating ligands on NAs can be precisely controlled by adjusting the molar ratio between the maleimide-modified ligand and the dendrimer. Furthermore, all the NAs were modified with similar copies of PEGs to minimize the interference from the nonuniform particle size or surface charge.

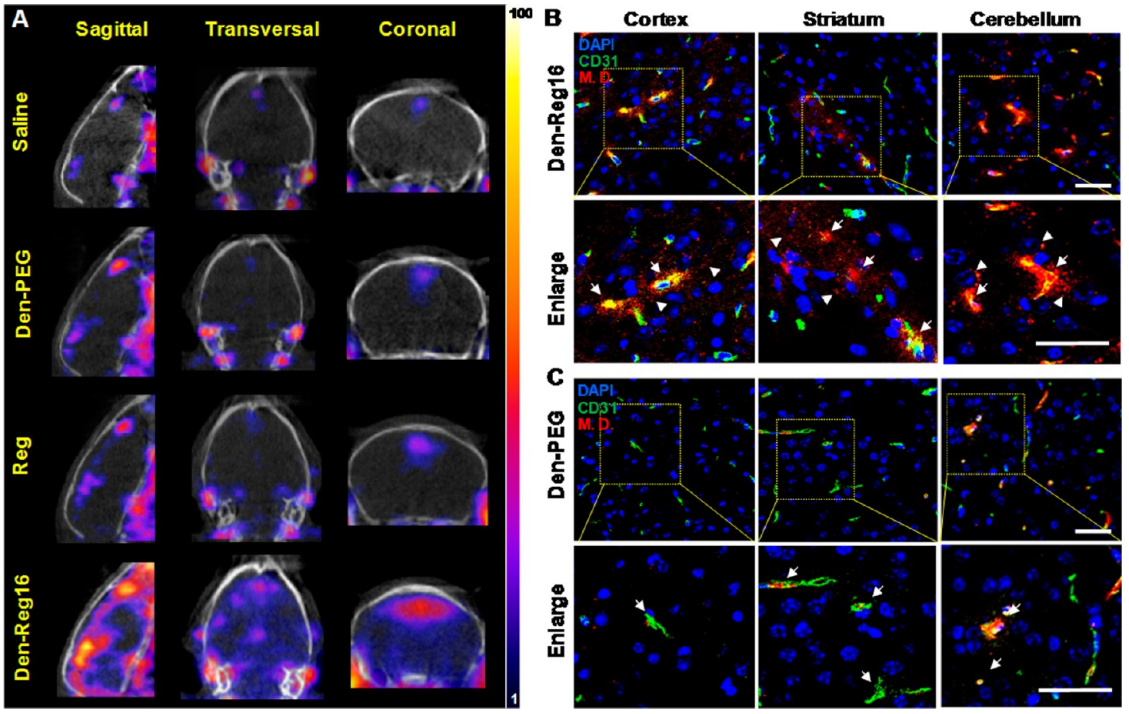

Figure 5. Brain drug delivery *via* NA-mediated AR signaling. (A) *In vivo* SPECT/CT images of mouse brain area when radioactive model drug (3.7×10^7 Bq/mouse) was injected at 30 min PI of 10 nmol NA, Reg, or saline *via* iv. Confocal fluorescence microscopic images of brain sections presenting cortex, striatum, and cerebellum areas when model drug was injected at 30 min PI of Den-Reg16 (B) or Den-PEG (C). CD31 immunofluorescence indicating brain vasculatures is displayed in green; model drug is displayed in red and DAPI-stained nuclei are blue. Yellow areas present the co-localized vessel and model drugs. Arrows point to the leaky vessels, and arrowheads point to the extravasated model drug. Scale bar, 50 μm.

The NA-dominated BBB permeability enhancement is evident with the ASF modulation, which is a prerequisite for the morphological alteration of endothelial cells (Figure 2C), and the TJ-associated protein attenuation, which indicates the loss of TJ tightness (Figure 2D). Compared to the monomeric agonist Reg, NAs led to a remarkably higher permeability of the BCEC monolayer and brain drug delivery efficiency *in vivo* (Figures 3−5). The above experimental results could be explained by (1) the prolonged circulation lifetime of NAs dramatically increasing the AR-activating opportunity; (2) the multivalent association between the NAs and the dimeric or even oligomeric receptor complexes on BCECs,[46,47] increasing AR binding avidity and specificity; (3) the multiply labeled ligands on NAs remodulating the orientation, stoichiometry, and aggregation pattern of ARs on cell membranes and hence amplifying signal transduction;[48] and (4) the labeled ligands on NAs triggering their concomitant binding to both orthostatic and allosteric sites of ARs, which up-regulates pharmacological responses with collateral efficacy.[34,49]

The capability of NAs to tune the BBB opening time-window may be attributed to the multivalent effect, which regulates the binding affinities between the NAs and ARs as well as the intracellular signal transduction efficacy. Joacobson *et al*. reported a series of agonist-labeled nanoparticles and found that the multivalent effect significantly increased their avidity to corresponding GPCRs, the signal transduction efficacy, and biological activities such as the inhibition of platelet aggregation[46] or cyclic AMP accumulation.[50] Because the multivalent effect depends on size, ligand substitution degree, and terminal functionality of nanoparticles, it is possible to fine-tune the BBB opening time-window by modulating the above factors. Considering the different pharmacokinetics of therapeutic compounds, NAs provide an unprecedented opportunity to maximize the brain drug delivery and minimize potential risk of overdosage by matching the BBB opening time-window and the drug circulation behavior.

In previous works, brain drug delivery efficiency was usually quantified by measuring the fluorescence intensity of mouse brain homogenization after the administration of a fluorophore-labeled model drug.[28] However, due to the autofluorescence from the endogenous proteins and the self-quenching of the fluorophores in the aqueous solution, the quantification of drug concentration *via* fluorimetric assay is not fully accurate. To overcome this problem, radioactive ^{99m}Tc-DTPA chelators were conjugated to the model drug, and its anatomic distribution and uptake efficiency in the brain can be noninvasively visualized and quantified by SPECT/CT. Additionally, taking advantage of optical imaging to simultaneously detect fluorescence signals with different wavelengths, the

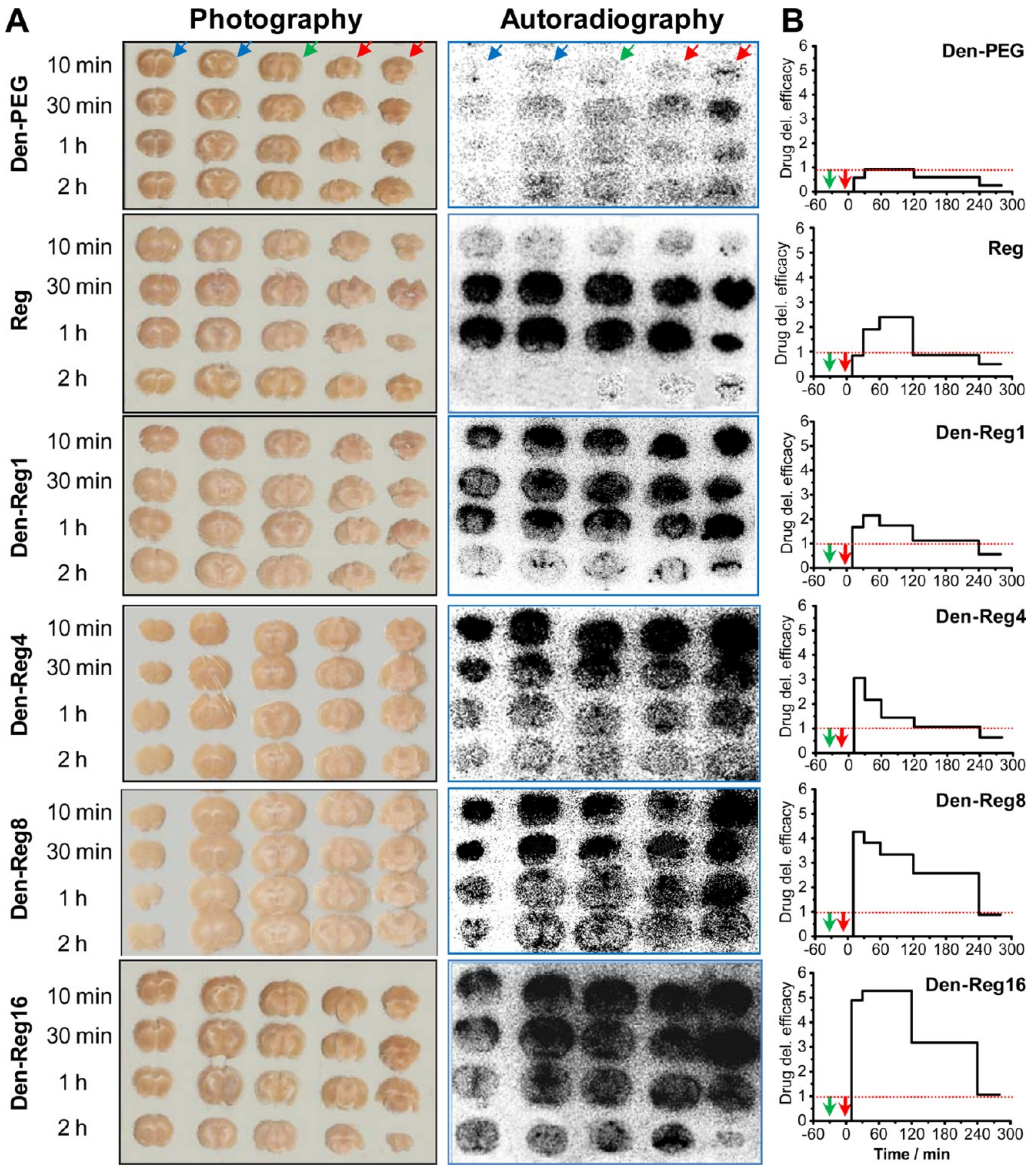

Figure 6. NA tuning of the BBB opening time-window. (A) Representative photographic and autoradiographic images of mouse brain sections when radioactive model drug (1.8×10^7 Bq/mouse) was injected at selected time-points postinjection of NAs or Reg (10 nmol/mouse). Blue, green, and red arrows point to the cortex, striatum, and cerebellum areas. (B) BBB opening time-window after single injection of NAs or Reg (10 nmol/mouse). The time-windows were determined by comparing the model drug brain uptakes at selected time-points after NA or Reg injection with the value after injection of saline as the negative control ($n = 4$). Green and red arrows indicate the time-points of NA and model drug injections. The red lines present the model drug brain uptake level with the pretreatment of saline.

labeling of different fluorophores on NAs and the model drug provides the possibility to monitor the cerebral distribution of NA and the model drug, respectively, and elucidate the mechanism of NA-mediated brain drug delivery.

Due to the expression of the A_{2A} AR in whole brain,[51] the main obstacle for the translation of NA-mediated brain drug delivery is how to specifically enhance BBB permeability in the lesion but not in the normal neurological tissues. In our previous work,[52] a two-order targeted brain tumor imaging strategy was put forward, in which the nanoprobes first target the tumor vasculatures. Increased local concentration of a nanoprobe in tumor sites facilitates its BBB crossing efficiency *via* receptor-mediated transcytosis (RMT). The BBB-traversed nanoprobes further target the cancer cells. By this strategy, brain tumor with a diameter of less than 1.0 mm was visualized with a high target to background ratio. Using the two-order targeting strategy, it is possible to label lesion targeting domains and agonist on the NAs. Because of the much higher binding affinity between the targeting domains and lesion-associated receptors (sub-nM to nM) than that between the labeled agonist and A_{2A} AR (sub-μM to μM), the dual-labeled NAs will hold the potential to specifically up-regulate BBB permeability at the lesion site, which benefits maximizing the therapeutic efficacy and minimizing the off-target side-effects.

CONCLUSION

In this work, we developed a series of NAs that not only up-regulated brain delivery of macromolecular model drugs by specifically signaling A_{2A} AR but also demonstrated the capability to temporarily tune the BBB opening time-window under *in vivo* conditions. This study shows that nanosized agonists have the ability to enhance brain drug delivery. Meanwhile, labeling the imaging reporter on the NAs and the model drug provides an unprecedented opportunity to noninvasively evaluate the BBB opening time-window, brain drug delivery efficiency, and therapeutic response. Overall, the NAs not only provide a new strategy to enhance brain drug delivery but also show promise to reduce potential risks such as overdosage and uncontrollable BBB leakage by tuning the BBB opening time-window according to the pharmacokinetic behavior of the therapeutics.

MATERIALS AND METHODS

Materials. All chemical reagents were obtained from Aladdin Reagent (Shanghai, China) unless otherwise specified. PAMAM G5 dendrimer (MW: 28 826 Da) was purchased from Dendritech Inc. (Midland, MI, USA). Rhodamine-NHS, fetal bovine serum (FBS), trypsin, penicillin, and streptomycin were purchased from Thermofisher Scientific (New York, USA). Rabbit anti-mouse ZO-1, A_{2A} AR and CD31 primary antibodies, and rhodamine-NHS were purchased from Invitrogen (Carlsbad, CA, USA). Alexa Fluo488-labeled goat anti-rabbit secondary antibody was purchased from Cell Signaling Technology (Danvers, MA, USA). Maleimide-PEG^{2k}-NHS and PEG-NHS were purchased from JenKem Technology Co. Ltd. (Beijing, China). IR783-NHS was prepared according to our previous work.[53] Amicon ultra-15 centrifugal filter tubes (10 000 MW cutoff) were from Millipore (Bedford, MA, USA).

Characterization. The molar ratios between dendrimer, PEG, and receptor-activating ligand in NAs were quantified by ^{1}H NMR (Varian Mercury400 spectrometer, USA). The labeling degree of fluorophores was calculated according to Lambert–Beer's law: $A = \varepsilon bc$ (A: absorbance, ε: extinction coefficient, b: thickness of the absorber, c: concentration). The absorbance of rhodamine ($\varepsilon_{552} = 60\,000\ M^{-1}cm^{-1}$) and IR783 ($\varepsilon_{754} = 169\,000\ M^{-1}\ cm^{-1}$) in NAs was measured on a UV-2401PC UV–vis spectrophotometer (Shimadzu, Japan). In the SDS-PAGE study, NAs in 30 μL of loading buffer were loaded on a 5% stacking gel that was set on a 10% resolving gel. Fluorescent images of the resolved SDS-PAGE gel were acquired in an IVIS Spectrum Imaging System (Caliper Life Sciences, USA). Hydrodynamic diameter and zeta potential of the NAs were obtained with a Malvern Zetasizer dynamic light scattering (Malvern Instruments Inc., USA).

Cell Culture. Murine brain endothelial cells bEnd.3 were purchased from the American Type Culture Collection (ATCC) and cultured in Dulbecco's modified Eagle's medium (DMEM, Gibco, USA) supplemented with 10% FBS, 2 mM L-glutamine, 1% penicillin, and streptomycin at 37 °C with 5% CO_2.

Western Blot Studies. bEnd.3 cells with 80% confluence were homogenized in lysis buffer containing protease inhibitors. Total protein (80 μg) was loaded on an 8% SDS-PAGE. After the electrophoresis, the gel was transferred to a nitrocellulose membrane, which was blocked, cut, and incubated with A_{2A} AR primary antibodies overnight. After washing thoroughly, the membranes were incubated with HRP-labeled goat anti-rabbit secondary antibody (1:20 000), developed by using the Supersignal West Pico chemiluminescent substrate kit (Pierce Biotechnology, USA) and exposed to X-ray film.

Competition Binding Studies. Competition assays were performed according to the reported protocol.[54] The bEnd.3 monolayer with 80% confluence was harvested, homogenized, and centrifuged. The isolated cell membranes were washed twice with cell binding buffer (50 mM Tris, 1 mM EDTA, pH 7.4) and then incubated overnight with ^{125}I-labeled ZM241385 in the presence of different concentrations of NAs. At the end of incubation, the unbound NA and ^{125}I-ZM241385 were removed by filtration through Whatman GF/C glass fiber filters. The membrane-bound radioactivity was then subjected to gamma-counting. The best-fit 50% inhibitory concentration (IC_{50}) values were calculated by fitting the data with nonlinear regression. Four determinations were performed for each concentration of the NAs.

F-Actin Staining of Endothelial Cells. bEnd.3 cells were seeded on four-well glass-bottom chamber slides (Thermofisher Scientific, USA) and incubated to reach 100% confluence. After treatment with 10 μM Reg or NA, the cells were washed, fixed with 4% paraformaldehyde (PFA), and then permeabilized with 0.3% Triton X-100. After blocking with 1% BSA for 1 h, slides were stained with phalloidin-Rho (Cytoskeleton, USA) followed by DAPI and mounted with cover-slides. Images were collected on a Zeiss LSM 710 META confocal laser scanning microscope (Carl Zeiss, Germany).

Transendothelial Cell Electrical Resistance Assay. bEnd.3 cells were seeded on the Transwell system (0.33 cm^2, pore size 1.0 μm, Corning Incorporated Life Sciences, USA) and cultured for 10–14 days before the experiment. TEER values were assessed using an epithelial voltohmmeter (MILLICELL-ERS, Millipore, USA). The cell monolayers were treated with 10 μM NAs or Reg for 45 min. At the end of treatment, the cells were washed and continually incubated. The TEER values of the cell monolayers were measured at 0 min, 15 min, 30 min, 60 min, 2 h, 4 h, 8 h, and 24 h after NA addition. Delivery of model drug across cell monolayers was quantified to evaluate NA-mediated permeability enhancement. After treatment with 10 μM NAs for 45 min, the monolayers were washed, and model drug (1 mg/mL, 45 kDa) was added to the apical chamber. At 8 h treatment with the NAs, rhodamine fluorescence intensity of the solution in the basal chamber was measured using a Shimazdu RF-5301PC spectrofluorophotometer (Shimadzu, Japan), and the monolayer crossing efficiency was calculated.

Animal Model. ICR mice and athymic nude mice 6–8 weeks old, weighing 20–22 g, were housed under specific pathogen-free conditions at the Department of Experimental Animals, Fudan University (Shanghai, China). All procedures were carried out in accordance with guidelines approved by the ethics committee of Fudan University (Shanghai, China).

***In Vivo* Optical Imaging Studies.** Optical images were acquired using an IVIS Spectrum in Vivo imaging system. Rhodamine fluorescence images were acquired using a red filter set (excitation filter: 495 nm; emission filter: 550–610 nm). NIR fluorescence images were acquired using an Integrin 750 filter set (excitation filter: 745 nm; emission filter: 800–840 nm). Dynamical fluorescence images were collected on nude mice with intact BBB after administration of NA (10 nmol) followed by the model drug (1.0 mg/mouse), which was injected at 30 min PI of NA. After *in vivo* imaging, the mice were perfused with saline followed by 4% PFA. Brains were carefully excised, and fluorescence images of whole brains were captured. Fluorescence intensities were quantified by the software provided by Caliper Life Sciences.

***In Vivo* SPECT/CT Imaging.** SPECT/CT imaging was performed on a Nano SPECT/CT Plus imager (Bioscan Inc., USA). Healthy ICR mice (20–22 g) were randomly divided into seven groups and injected iv with 10 nmol of NA, saline, or Reg. Thirty minutes after NA injection, 3.7×10^7 Bq DTPA-^{99m}Tc-labeled model drug was administered *via* iv. At 30 min PI, the mice were anesthetized by inhalation of 2% isoflurane in oxygen, and SPECT/CT images were collected. A total of 24 projections were acquired

with a minimum of 40 000 counts per projection. Prior to each SPECT imaging, cone-beam CT (180 projections, 55 kVp, 147 μA) images were acquired. The whole procedure of SPECT/CT scanning took 35 min per animal, and the fusion images were obtained using the automatic fusion feature of the In Vivo Scope software.

Immunohistochemistry Staining. For cell culture studies, bEnd.3 cells seeded on four-well chamber slides were incubated to allow the confluence to reach greater than 100%. After the treatment with NA (10 μM) for 45 min, the cells were washed, fixed, blocked, and stained with rabbit anti-mouse ZO-1 primary antibody followed by Alexa-Fluoro488-labeled goat anti-rabbit secondary antibody. The nuclei were stained with DAPI, and the slides were mounted for imaging. For *ex vivo* tissue studies, mouse brains were harvested, fixed, dehydrated, sectioned with a thickness of 10.0 μm, and immunostained with CD31 primary antibody and Alexa-Fluoro488-labeled secondary antibody followed by nuclear staining.

Confocal Fluorescence Microscopic Imaging. Fluorescence microscopic images were collected on a Zeiss LSM 710 META confocal laser scanning microscope (Carl Zeiss, Germany) by using a 20× or 40× lens. DAPI was excited with a 405 nm laser, and the emission was detected with a photomultiplier by a 420−480 nm band-pass filter. Alexa-Flour488 was excited with a 495 nm laser, and emission was detected by a second photomultiplier using a 505−550 nm band-pass filter. Rhodamine was excited with a 543 nm laser, and the emission was detected by a third photomultiplier using a 560 nm band-pass filter. The fluorescence images were processed by ZEN 2012 software (Carl Zeiss, Germany).

Autoradiography Studies. ICR mice were randomly divided into seven groups. At 10 min, 30 min, 1 h, 2 h, or 4 h PI of saline, NA (10 nmol), or Reg (10 nmol) *via* iv, DTPA-^{99m}Tc-labeled model drug (1.8×10^7 Bq/mouse) was administrated *via* iv. Thirty minutes after drug injection, the mice were scarified and the brains were excised, prefixed, and sectioned coronally with a thickness of 2.0 mm. The brain sections were exposed to a phosphor storage screen film (super-resolution screen; PerkinElmer) for 24 h. Reading of the screens by a Cyclone Pulse Storage Phosphor system (PerkinElmer, USA) gave autoradiography images, which were further analyzed by using Optiquant software (PerkinElmer). Meanwhile, photographic images of the brain sections were taken by a Leica MZ75 high-performance stereomicroscope (Leica Inc., Germany).

Biodistribution Studies. ICR mice with intact BBBs were randomly divided into seven groups and injected with 10 nmol of NAs or Reg *via* iv. At 30 min PI, DTPA-^{99m}Tc-labeled model drug (3.7×10^6 Bq/mouse) was administrated *via* iv. Thirty minutes post model drug injection, the mice were sacrificed and perfused with PBS. Selected organs including brain were isolated and weighed, and the radioactivity was counted with an automatic γ-counter. Decay of radioactivity was corrected as follows: corrected radioactivity = measured activity × exp(ln[2] × interval/6.02). The biodistribution data were presented as a percentage of the injected radioactivity per gram (%ID/g).

Statistical Analysis. Quantified data are presented as mean ± SD when the sample number was above 4 ($n > 4$).

Conflict of Interest: The authors declare no competing financial interest.

Supporting Information Available: Details of model drug synthesis and characterization, Figures S1−S7, NMR and MS spectra. This material is available free of charge *via* the Internet at http://pubs.acs.org.

Acknowledgment. This work was supported by the National Basic Research Program of China (973 Program, 2013CB733801, 2013CB932500), the National Natural Science Foundation of China (Nos. 81371624, 81171384), New Century Excellent Talents in University Award, and the Shanghai Foundation for Development of Science and Technology (Nos. 13NM1400400, 12NM0501400).

REFERENCES AND NOTES

1. Zlokovic, B. V. The Blood-Brain Barrier in Health and Chronic Neurodegenerative Disorders. *Neuron* **2008**, *57*, 178–201.
2. Ghose, A. K.; Viswanadhan, V. N.; Wendoloski, J. J. A Knowledge-Based Approach in Designing Combinatorial or Medicinal Chemistry Libraries for Drug Discovery. 1. A Qualitative and Quantitative Characterization of Known Drug Databases. *J. Comb. Chem.* **1999**, *1*, 55–68.
3. Daneman, R. The Blood-Brain Barrier in Health and Disease. *Ann. Neurol.* **2012**, *72*, 648–672.
4. Abbott, N. J.; Patabendige, A. A.; Dolman, D. E.; Yusof, S. R.; Begley, D. J. Structure and Function of the Blood-Brain Barrier. *Neurobiol. Dis.* **2010**, *37*, 13–25.
5. Huber, J. D.; Egleton, R. D.; Davis, T. P. Molecular Physiology and Pathophysiology of Tight Junctions in the Blood-Brain Barrier. *Trends Neurosci.* **2001**, *24*, 719–725.
6. Pardridge, W. M. The Blood-Brain Barrier: Bottleneck in Brain Drug Development. *Neurorx* **2005**, *2*, 3–14.
7. Lipinski, C. A. Drug-Like Properties and the Causes of Poor Solubility and Poor Permeability. *J. Pharmacol. Toxicol. Methods* **2000**, *44*, 235–249.
8. Sarin, H.; Kanevsky, A. S.; Wu, H.; Sousa, A. A.; Wilson, C. M.; Aronova, M. A.; Griffiths, G. L.; Leapman, R. D.; Vo, H. Q. Physiologic Upper Limit of Pore Size in the Blood-Tumor Barrier of Malignant Solid Tumors. *J. Transl. Med.* **2009**, *7*, 51.
9. Gao, X.; Li, C. Nanoprobes Visualizing Gliomas by Crossing the Blood Brain Tumor Barrier. *Small* **2013**, DOI: 10.1002/smll.201301673.
10. Jiang, Q.; Ewing, J. R.; Chopp, M. MRI of Blood-Brain Barrier Permeability in Cerebral Ischemia. *Transl. Stroke Res.* **2012**, *3*, 56–64.
11. Belayev, L.; Busto, R.; Zhao, W.; Ginsberg, M. D. Quantitative Evaluation of Blood-Brain Barrier Permeability Following Middle Cerebral Artery Occlusion in Rats. *Brain Res.* **1996**, *739*, 88–96.
12. Bowman, G. L.; Kaye, J. A.; Moore, M.; Waichunas, D.; Carlson, N. E.; Quinn, J. F. Blood-Brain Barrier Impairment in Alzheimer Disease: Stability and Functional Significance. *Neurology* **2007**, *68*, 1809–1814.
13. Weiss, N.; Miller, F.; Cazaubon, S.; Couraud, P. O. The Blood-Brain Barrier in Brain Homeostasis and Neurological Diseases. *Biochim. Biophys. Acta* **2009**, *1788*, 842–857.
14. Lee, G.; Dallas, S.; Hong, M.; Bendayan, R. Drug Transporters in the Central Nervous System: Brain Barriers and Brain Parenchyma Considerations. *Pharmacol. Rev.* **2001**, *53*, 569–596.
15. Liu, H. L.; Hua, M. Y.; Chen, P. Y.; Chu, P. C.; Pan, C. H.; Yang, H. W.; Huang, C. Y.; Wang, J. J.; Yen, T. C.; Wei, K. C. Blood-Brain Barrier Disruption with Focused Ultrasound Enhances Delivery of Chemotherapeutic Drugs for Glioblastoma Treatment. *Radiology* **2010**, *255*, 415–425.
16. Bobo, R. H.; Laske, D. W.; Akbasak, A.; Morrison, P. F.; Dedrick, R. L.; Oldfield, E. H. Convection-Enhanced Delivery of Macromolecules in the Brain. *Proc. Natl. Acad. Sci. U.S.A.* **1994**, *91*, 2076–2080.
17. Allard, E.; Passirani, C.; Benoit, J. P. Convection-Enhanced Delivery of Nanocarriers for the Treatment of Brain Tumors. *Biomaterials* **2009**, *30*, 2302–2318.
18. Rapoport, S. I. Osmotic Opening of the Blood-Brain Barrier: Principles, Mechanism, and Therapeutic Applications. *Cell. Mol. Neurobiol.* **2000**, *20*, 217–230.
19. Neuwelt, E. A.; Barnett, P. A.; Glasberg, M.; Frenkel, E. P. Pharmacology and Neurotoxicity of Cis-Diamminedichloroplatinum, Bleomycin, 5-Fluorouracil, and Cyclophosphamide Administration Following Osmotic Blood-Brain Barrier Modification. *Cancer Res.* **1983**, *43*, 5278–5285.
20. Marchi, N.; Angelov, L.; Masaryk, T.; Fazio, V.; Granata, T.; Hernandez, N.; Hallene, K.; Diglaw, T.; Franic, L.; Najm, I.; *et al.* Seizure-Promoting Effect of Blood-Brain Barrier Disruption. *Epilepsia* **2007**, *48*, 732–742.
21. Hynynen, K. Ultrasound for Drug and Gene Delivery to the Brain. *Adv. Drug Delivery Rev.* **2008**, *60*, 1209–1217.
22. Kinoshita, M.; McDannold, N.; Jolesz, F. A.; Hynynen, K. Noninvasive Localized Delivery of Herceptin to the Mouse Brain by Mri-Guided Focused Ultrasound-Induced Blood-Brain Barrier Disruption. *Proc. Natl. Acad. Sci. U.S.A.* **2006**, *103*, 11719–11723.

23. Tuma, P.; Hubbard, A. L. Transcytosis: Crossing Cellular Barriers. *Physiol. Rev.* **2003**, *83*, 871–932.
24. Herve, F.; Ghinea, N.; Scherrmann, J. M. CNS Delivery via Adsorptive Transcytosis. *AAPS J.* **2008**, *10*, 455–472.
25. Zensi, A.; Begley, D.; Pontikis, C.; Legros, C.; Mihoreanu, L.; Wagner, S.; Buchel, C.; von Briesen, H.; Kreuter, J. Albumin Nanoparticles Targeted with Apo E Enter the CNS by Transcytosis and Are Delivered to Neurones. *J. Controlled Release* **2009**, *137*, 78–86.
26. Yan, H.; Wang, J.; Yi, P.; Lei, H.; Zhan, C.; Xie, C.; Feng, L.; Qian, J.; Zhu, J.; Lu, W.; *et al*. Imaging Brain Tumor by Dendrimer-Based Optical/Paramagnetic Nanoprobe across the Blood-Brain Barrier. *Chem. Commun.* **2011**, *47*, 8130–8132.
27. Jacobson, K. A.; Gao, Z. G. Adenosine Receptors as Therapeutic Targets. *Nat. Rev. Drug Discovery* **2006**, *5*, 247–264.
28. Carman, A. J.; Mills, J. H.; Krenz, A.; Kim, D. G.; Bynoe, M. S. Adenosine Receptor Signaling Modulates Permeability of the Blood-Brain Barrier. *J. Neurosci.* **2011**, *31*, 13272–13280.
29. Sohail, M. A.; Hashmi, A. Z.; Hakim, W.; Watanabe, A.; Zipprich, A.; Groszmann, R. J.; Dranoff, J. A.; Torok, N. J.; Mehal, W. Z. Adenosine Induces Loss of Actin Stress Fibers and Inhibits Contraction in Hepatic Stellate Cells via Rho Inhibition. *Hepatology* **2009**, *49*, 185–194.
30. de Lera Ruiz, M.; Lim, Y.-H.; Zheng, J. Adenosine A2a Receptor as a Drug Discovery Target. *J. Med. Chem.* **2013**, 10.1021/jm4011669.
31. Albanese, A.; Tang, P. S.; Chan, W. C. The Effect of Nanoparticle Size, Shape, and Surface Chemistry on Biological Systems. *Annu. Rev. Biomed. Eng.* **2012**, *14*, 1–16.
32. Willmann, J. K.; van Bruggen, N.; Dinkelborg, L. M.; Gambhir, S. S. Molecular Imaging in Drug Development. *Nat. Rev. Drug Discovery* **2008**, *7*, 591–607.
33. Barrett, T.; Ravizzini, G.; Choyke, P. L.; Kobayashi, H. Dendrimers in Medical Nanotechnology. *IEEE Eng. Med. Biol. Mag.* **2009**, *28*, 12–22.
34. Choi, J. J.; Wang, S.; Tung, Y. S.; Morrison, B., 3rd; Konofagou, E. E. Molecules of Various Pharmacologically-Relevant Sizes Can Cross the Ultrasound-Induced Blood-Brain Barrier Opening in Vivo. *Ultrasound Med. Biol.* **2010**, *36*, 58–67.
35. Armulik, A.; Genove, G.; Mae, M.; Nisancioglu, M. H.; Wallgard, E.; Niaudet, C.; He, L.; Norlin, J.; Lindblom, P.; Strittmatter, K.; *et al*. Pericytes Regulate the Blood-Brain Barrier. *Nature* **2010**, *468*, 557–561.
36. Caulkett, P. W. R.; Jones, G.; McPartlin, M.; Renshaw, N. D.; Stewart, S. K.; Wright, B. Adenine Isosteres with Bridgehead Nitrogen. Part 1. Two Independent Syntheses of the [1,2,4]Triazolo[1,5-a][1,3,5]Triazine Ring System Leading to a Range of Substituents in the 2, 5 and 7 Positions. *J. Chem. Soc., Perkins Trans. 1* **1995**, 801–808.
37. Neuwelt, E. A.; Frenkel, E. P.; D'Agostino, A. N.; Carney, D. N.; Minna, J. D.; Barnett, P. A.; McCormick, C. I. Growth of Human Lung Tumor in the Brain of the Nude Rat as a Model to Evaluate Antitumor Agent Delivery across the Blood-Brain Barrier. *Cancer Res.* **1985**, *45*, 2827–2833.
38. Daneman, R.; Zhou, L.; Kebede, A. A.; Barres, B. A. Pericytes Are Required for Blood-Brain Barrier Integrity during Embryogenesis. *Nature* **2010**, *468*, 562–566.
39. Dixon, A. K.; Gubitz, A. K.; Sirinathsinghji, D. J.; Richardson, P. J.; Freeman, T. C. Tissue Distribution of Adenosine Receptor Mrnas in the Rat. *Br. J. Pharmacol.* **1996**, *118*, 1461–1468.
40. Thal, S. C.; Luh, C.; Schaible, E. V.; Timaru-Kast, R.; Hedrich, J.; Luhmann, H. J.; Engelhard, K.; Zehendner, C. M. Volatile Anesthetics Influence Blood-Brain Barrier Integrity by Modulation of Tight Junction Protein Expression in Traumatic Brain Injury. *PLoS One* **2012**, *7*, e50752.
41. Kobzik, L. Lung Macrophage Uptake of Unopsonized Environmental Particulates. Role of Scavenger-Type Receptors. *J. Immunol.* **1995**, *155*, 367–376.
42. Yang, J.; Wadghiri, Y. Z.; Hoang, D. M.; Tsui, W.; Sun, Y.; Chung, E.; Li, Y.; Wang, A.; de Leon, M.; Wisniewski, T. Detection of Amyloid Plaques Targeted by Uspio-Abeta1-42 in Alzheimer's Disease Transgenic Mice Using Magnetic Resonance Microimaging. *Neuroimage* **2011**, *55*, 1600–1609.
43. Wang, M.; Etu, J.; Joshi, S. Enhanced Disruption of the Blood Brain Barrier by Intracarotid Mannitol Injection during Transient Cerebral Hypoperfusion in Rabbits. *J. Neurosurg. Anesthesiol.* **2007**, *19*, 249–256.
44. Elzein, E.; Kalla, R.; Li, X.; Perry, T.; Marquart, T.; Micklatcher, M.; Li, Y.; Wu, Y.; Zeng, D.; Zablocki, J. N6-Cycloalkyl-2-Substituted Adenosine Derivatives as Selective, High Affinity Adenosine A1 Receptor Agonists. *Bioorg. Med. Chem. Lett.* **2007**, *17*, 161–166.
45. Bryantsev, V. S.; Diallo, M. S.; Goddard, W. A., 3rd. pK_a Calculations of Aliphatic Amines, Diamines, and Aminoamides via Density Functional Theory with a Poisson-Boltzmann Continuum Solvent Model. *J. Phys. Chem. A* **2007**, *111*, 4422–4430.
46. Kim, Y.; Hechler, B.; Klutz, A. M.; Gachet, C.; Jacobson, K. A. Toward Multivalent Signaling across G Protein-Coupled Receptors from Poly(Amidoamine) Dendrimers. *Bioconjugate Chem.* **2008**, *19*, 406–411.
47. Tosh, D. K.; Yoo, L. S.; Chinn, M.; Hong, K.; Kilbey, S. M., 2nd; Barrett, M. O.; Fricks, I. P.; Harden, T. K.; Gao, Z. G.; Jacobson, K. A. Polyamidoamine (PAMAM) Dendrimer Conjugates of "Clickable" Agonists of the A3 Adenosine Receptor and Coactivation of the P2y14 Receptor by a Tethered Nucleotide. *Bioconjugate Chem.* **2010**, *21*, 372–384.
48. Kiessling, L. L.; Gestwicki, J. E.; Strong, L. E. Synthetic Multivalent Ligands as Probes of Signal Transduction. *Angew. Chem., Int. Ed.* **2006**, *45*, 2348–2368.
49. Leach, K.; Sexton, P. M.; Christopoulos, A. Allosteric GPCR Modulators: Taking Advantage of Permissive Receptor Pharmacology. *Trends Pharmacol. Sci.* **2007**, *28*, 382–389.
50. Das, A.; Zhou, Y.; Ivanov, A. A.; Carter, R. L.; Harden, T. K.; Jacobson, K. A. Enhanced Potency of Nucleotide-Dendrimer Conjugates as Agonists of the P2y14 Receptor: Multivalent Effect in G Protein-Coupled Receptor Recognition. *Bioconjugate Chem.* **2009**, *20*, 1650–1659.
51. Ribeiro, J. A.; Sebastiao, A. M.; de Mendonca, A. Adenosine Receptors in the Nervous System: Pathophysiological Implications. *Prog. Neurobiol.* **2002**, *68*, 377–392.
52. Yan, H.; Wang, L.; Wang, J.; Weng, X.; Lei, H.; Wang, X.; Jiang, L.; Zhu, J.; Lu, W.; Wei, X.; *et al*. Two-Order Targeted Brain Tumor Imaging by Using an Optical/Paramagnetic Nanoprobe across the Blood Brain Barrier. *ACS Nano* **2012**, *6*, 410–420.
53. Li, C.; Winnard, P., Jr.; Bhujwalla, Z. M. Facile Synthesis of 1-(Acetic Acid)-4,7,10-Tris(tert-Butoxycarbonylmethyl)-1,4,7,10-Tetraaza-Cyclododecane: A Reactive Precursor Chelating Agent. *Tetrahedron Lett.* **2009**, *50*, 2929–2931.
54. Alexander, S. P.; Millns, P. J. [(3)H]Zm241385—an Antagonist Radioligand for Adenosine a(2a) Receptors in Rat Brain. *Eur. J. Pharmacol.* **2001**, *411*, 205–210.